

STRONG EXCESS FARADAY ROTATION ON THE INSIDE OF THE SAGITTARIUS SPIRAL ARM

R. SHANAHAN¹, S. J. LEMMER¹, J. M. STIL¹, H. BEUTHER², Y. WANG², J. SOLER², L. D. ANDERSON^{3,4,5}, F. BIGIEL⁶,
 S. C. O. GLOVER⁷, P. GOLDSMITH⁸, R. S. KLESSEN^{7,9}, N. M. MCCLURE-GRIFFITHS¹⁰, S. REISSL⁷, M. RUGEL¹¹,
 AND R. J. SMITH¹²

¹Department of Physics and Astronomy, The University of Calgary, 2500 University Drive NW, Calgary AB T2N 1N4, Canada

²Max Planck Institute for Astronomy, Königstuhl 17, 69117 Heidelberg, Germany

³Department of Physics and Astronomy, West Virginia University, Morgantown, WV 26506, USA

⁴Adjunct Astronomer at the Green Bank Observatory, PO Box 2, Green Bank, WV 24944, USA

⁵Center for Gravitational Waves and Cosmology, West Virginia University, Chestnut Ridge Research Building, Morgantown, WV 26505, USA

⁶Argelander-Institute for Astronomy, University of Bonn, Auf dem Hügel 71, 53121 Bonn, Germany

⁷Universität Heidelberg, Zentrum für Astronomie, Institut für Theoretische Astrophysik, Albert-Ueberle-Str. 2, D-69120 Heidelberg, Germany

⁸Jet Propulsion Laboratory, California Institute of Technology, 4800 Oak Grove Drive, Pasadena, CA 91109, USA

⁹Universität Heidelberg, Interdisziplinäres Zentrum für Wissenschaftliches Rechnen, Im Neuenheimer Feld 205, 69120 Heidelberg, Germany

¹⁰Research School of Astronomy and Astrophysics, The Australian National University, Canberra, ACT, Australia

¹¹Max-Planck-Institut für Radioastronomie, Auf dem Hügel 69, 53121 Bonn, Germany

¹²Jodrell Bank Centre for Astrophysics, School of Physics and Astronomy, The University of Manchester, Oxford Road, Manchester, M13 9PL, UK

ABSTRACT

We present first results for Faraday rotation of compact polarized sources (1 to 2 GHz continuum) in The HI/OH/Recombination line (THOR) survey of the inner Galaxy. In the Galactic longitude range $39^\circ < \ell < 52^\circ$, we find rotation measures in the range $-310 \text{ rad m}^{-2} \leq RM \leq +4219 \text{ rad m}^{-2}$, with the highest values concentrated within a degree of $\ell = 48^\circ$ at the Sagittarius arm tangent. Most of the high RM s arise in diffuse plasma, along lines of sight that do not intersect H II regions. For $\ell > 49^\circ$, RM drops off rapidly, while at $\ell < 47^\circ$, the mean RM is higher with a larger standard deviation than at $\ell > 49^\circ$. We attribute the RM structure to the compressed diffuse Warm Ionized Medium in the spiral arm, upstream of the major star formation regions. The Sagittarius arm acts as a significant Faraday screen inside the Galaxy. This has implications for models of the Galactic magnetic field and the expected amount of Faraday rotation of Fast Radio Bursts from their host galaxies. We emphasize the importance of sensitivity to high Faraday depth in future polarization surveys.

1. INTRODUCTION

Magnetic fields play an important role in the physics of the interstellar medium on a wide range of scales (e.g. Beck 2015). Plasma ejected by stellar winds and supernova explosions expands into the surrounding magnetized interstellar medium to form magnetized super bubbles (e.g. Ferrière et al. 1991; Tomisaka 1998; Stil et al. 2009), driving a complex feedback cycle between star formation and the magnetic field. The strength and structure of the magnetic field are important for understanding its origin and effect on the interstellar medium (Klessen & Glover 2016). On a Galactic scale the magnetic field is best observed through Faraday rotation of radio waves, by which the polarization angle θ of a linearly polarized source changes with wavelength, λ , ac-

ording to $\Delta\theta = \phi\lambda^2$. The Faraday depth ϕ is defined as

$$\phi = \frac{e^3}{2\pi m_e^2 c^4} \int n_e B_{\parallel} dl = 0.81 \int \left(\frac{n_e}{\text{cm}^{-3}} \right) \left(\frac{B_{\parallel}}{\mu\text{G}} \right) \left(\frac{dl}{\text{pc}} \right), \quad (1)$$

with ϕ in rad m^{-2} , c the speed of light, n_e the density of free electrons (mass m_e , charge $-e$), B_{\parallel} the component of the magnetic field along the line of sight, and l the distance along the line of sight (Klein & Fletcher 2015). The integral is evaluated from the source to the observer such that positive ϕ corresponds to B_{\parallel} toward the observer. Rotation measure RM is the slope of the relation between $\Delta\theta$ and λ^2 . In its simplest form, $RM = \phi$, but superposition of waves that experience different amounts of Faraday rotation can make RM a function of wave-

length and different from ϕ (e.g. Sokoloff et al. 1998).

Most Galactic Faraday rotation is believed to originate in the Warm Ionized Medium (WIM) (Heiles & Haverkorn 2012). Observable Faraday rotation can arise from a plasma whose free-free continuum and spectral line emission are undetectable (Uyaniker et al. 2003), yet inversion of the integral in Equation 1 requires assumptions about the geometry, electron density and the magnetic field configuration in the object. In case of the Galactic magnetic field, this inversion benefits from a unique combination of measurements along diverging lines of sight, and information about n_e from pulsar dispersion measure DM ,

$$DM = \int n_e dl, \quad (2)$$

with DM measured in pc cm^{-3} , and n_e and l in the same units as in Equation 1. Pulsar DM s indicate a higher plasma density in the spiral arms, but the sampling is not yet dense enough to map structures on smaller scales consistently (Taylor & Cordes 1993; Cordes & Lazio 2002).

Large sections of the Milky Way disk have been surveyed for polarization of extragalactic sources and pulsars to map the Galactic magnetic field (e.g. Broten et al. 1988; Clegg et al. 1992; Brown & Taylor 2001; Brown et al. 2003, 2007; Taylor et al. 2009; Han et al. 2018; Schnitzeler et al. 2019), and converted into complete maps of Galactic Faraday rotation by Oppermann et al. (2012), Oppermann et al. (2015), and Hutschenreuter & Ensslin (2019). The inner first Galactic quadrant is covered relatively sparsely by the survey of Van Eck et al. (2011) that targeted polarized sources selected from the NVSS (Condon et al. 1998). Jansson & Farrar (2012) combined Faraday rotation through the disk and the halo with polarization of diffuse emission into a coherent model of the large-scale Galactic magnetic field. This large-scale field has a strength of a few μG and a direction that varies with distance from the Galactic centre. The number of reversals and the precise geometry of the Galactic magnetic field is still a matter of debate (e.g. Brown et al. 2007; Han et al. 2018).

The contribution of spiral arms to the Faraday depth of the Galaxy affects the geometry and field strength in the remainder of the disk. Brown & Taylor (2001) discussed deviations in RM in the direction of H II regions along the local Orion-Cygnus arm. Vallée et al. (1988) reported excess Faraday rotation of -75 rad m^{-2} in the region of the Scutum arm tangent. In this paper we present the first results of Faraday rotation of compact polarized sources from the THOR survey in the region of the Sagittarius (Sgr) arm tangent.

2. OBSERVATIONS AND METHODS

The THOR survey (Beuther et al. 2016) covers the inner Galaxy in the longitude range $14^\circ 5' < \ell < 67^\circ 4'$ and latitude $-1^\circ 25' < b < 1^\circ 25'$ with the Karl G. Jansky Very Large Array (VLA) in C configuration in L band (1 - 2 GHz). The survey includes the 21-cm line of atomic hydrogen, OH lines, several radio recombination lines and the continuum in 512 channels from 1 to 2 GHz. The 21-cm line and total intensity continuum were combined with archival data from the VLA Galactic Plane Survey (VGPS; Stil et al. 2006) and the Effelsberg continuum survey by Reich et al. (1990) at 1.4 GHz only. For the other spectral lines and continuum polarization, only the C-configuration data exist, sampling the continuum at 1.5 GHz on angular scales from $\sim 5'$ to $\sim 15''$.

Radio Frequency Interference (RFI) flagging and standard flux and phase calibration of the continuum data were described by Beuther et al. (2016). Polarization calibration and imaging was done in CASA following standard procedures. The single phase calibrator observed during an observing session was used for polarization calibration, with 3C286 used for polarization angle calibration. The visibilities were averaged into 8 MHz channels before imaging of Stokes I , Q , and U to reduce data volume and improve the signal to noise ratio per channel for cleaning. The noise is approximately $0.4 \text{ mJy beam}^{-1}$ per 8 MHz channel. Bühr et al. (2016) and Wang et al. (2018) compiled a list of compact continuum sources in the THOR survey. Sources with peak brightness more than 10 mJy beam^{-1} were selected for polarization analysis. The input catalog is essentially complete at 10 mJy , but detection of the polarized signal depends on the local noise level, which can be raised by nearby bright diffuse emission. Our sample includes additional polarized components of resolved sources, but excludes occasional entries that were considered a part of bright diffuse sources after visual inspection. No other selection was made, but we follow the common implicit assumption that compact sources detected in polarization are extragalactic. Pulsars are rarely detectable in cm continuum imaging surveys such as the THOR continuum catalog (e.g. Dai et al. 2016).

Analysis of the THOR polarization image cubes begins with Faraday Rotation Measure Synthesis (RM synthesis, Brentjens & De Bruyn 2005). The complex polarization \mathcal{P} as a function of wavelength λ is expressed in terms of the normalized Stokes parameters $q = Q/I$ and $u = U/I$ as $\mathcal{P} = q + iu$. The dimensionless Faraday depth spectrum $\tilde{\mathcal{F}}(\phi)$ is obtained by the Fourier transform

$$\tilde{\mathcal{F}}(\phi) = \int_{-\infty}^{\infty} \mathcal{P}(\xi) W(\xi) \exp[-2\pi i \phi \xi] d\xi, \quad (3)$$

where $\xi = \lambda^2$ for $\xi > 0$ and the weight function $W(\xi) = 0$ where no measurements exist, including $\xi < 0$.

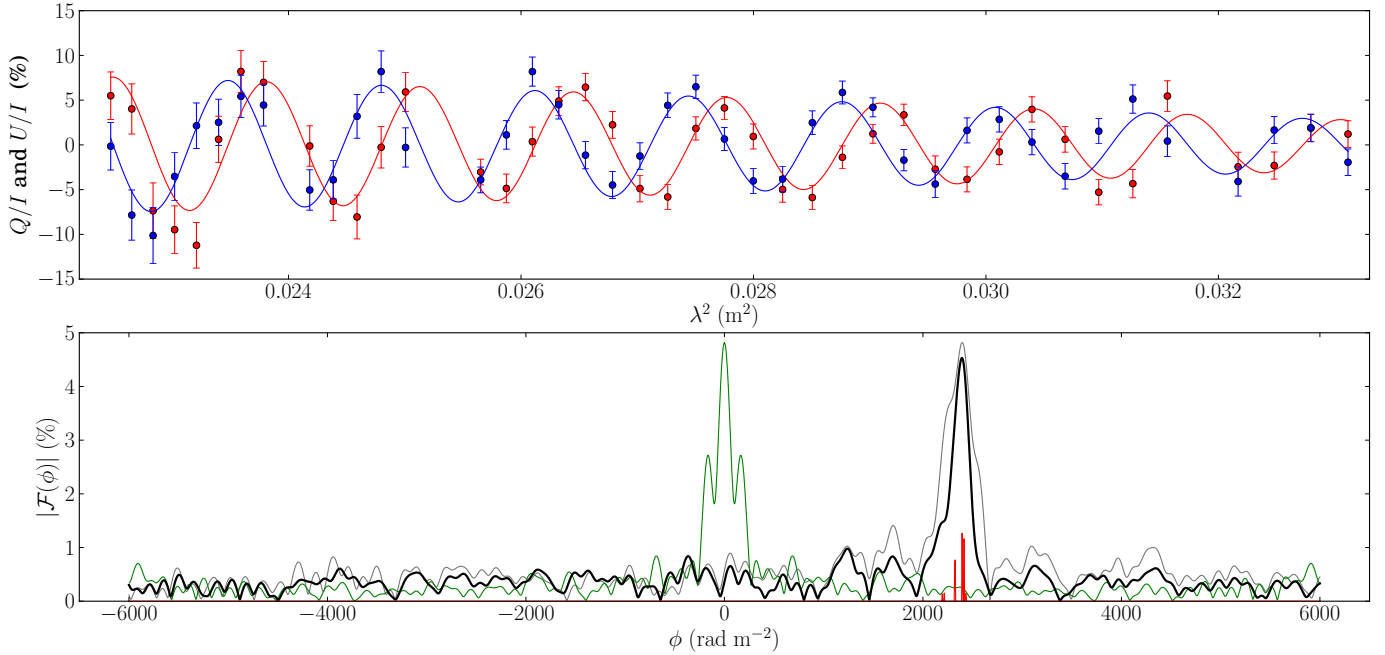


Figure 1. Faraday rotation of G48.561–0.364, the fifth highest RM in the sample. The top panel shows Stokes Q (blue) and U (red) as a function of λ^2 with the result of QU fitting, adopting a depolarizing turbulent foreground screen model with Faraday depth dispersion σ_ϕ , $\mathcal{P} = \mathcal{P}_0 \exp[-2\sigma_\phi^2 \lambda^4 - 2i\phi\lambda^2]$ (Sokoloff et al. 1998). The bottom panel shows the dirty Faraday depth spectrum (grey), the RMTF with amplitude scaled to the strength of the signal (green, centered on $\phi = 0 \text{ rad m}^{-2}$), the RM Clean deconvolved Faraday depth spectrum $|\mathcal{F}|$ (black) and RM clean components in red.

Multiple values of ϕ can arise from blending different rates of Faraday rotation, by integrating over frequency, solid angle, or different emission regions along the line of sight. This is referred to as Faraday complexity. It gives rise to fractional polarization changing with wavelength, and a non-linear relation between polarization angle and λ^2 . The Rotation Measure Transfer Function (RMTF) serves as the point spread function in Faraday depth. It is the Fourier transform of the function $W(\xi)$. RFI flagging reduces Faraday depth resolution to 101 rad m^{-2} in the median and raises the side lobes of the $RMTF$, as shown in Figure 1.

Significant Faraday rotation within a single frequency channel leads to depolarization. If the width of a channel in λ^2 is expressed as $\delta\lambda^2$, the maximum observable Faraday depth is (Brentjens & De Bruyn 2005),

$$|\phi_{\max}| = \frac{\sqrt{3}}{\delta\lambda^2}. \quad (4)$$

For 8 MHz channels at 1.5 GHz this amounts to $|\phi_{\max}| = 4.0 \times 10^3 \text{ rad m}^{-2}$, and at 1.8 GHz to $|\phi_{\max}| = 7.1 \times 10^3 \text{ rad m}^{-2}$, so we have sensitivity to somewhat higher Faraday depth from the highest observed frequencies, with reduced sensitivity because of the smaller effective bandwidth (cf. Pratley & Johnston-Hollitt 2019).

In this first exploration of the polarization survey, we present Faraday rotation of compact polarized extra-

galactic sources in the longitude range $39^\circ < \ell < 52^\circ$, and Faraday depth in the range $-6000 \text{ rad m}^{-2} < \phi < 6000 \text{ rad m}^{-2}$. In view of the high RM s encountered for $47^\circ < \ell < 49^\circ$, this region was also analyzed at full spectral resolution (2 MHz channels between 1.6 and 1.9 GHz) up to $|\phi_{\max}| = 2.5 \times 10^4 \text{ rad m}^{-2}$. No detections were found outside the initial search range, but three more high RM sources were added to the sample. Sources detected in polarization were analyzed with the RM Clean algorithm (Heald 2009) and QU fitting (Law et al. 2011), using the `RMtools`¹ package of C. Purcell. Conceptually, RM synthesis resembles imaging of the visibilities in radio interferometry followed by a Clean deconvolution, while QU fitting resembles fitting a source in the visibility plane.

3. RESULTS

We present RM s for 127 compact polarized sources detected in the longitude range $39^\circ < \ell < 52^\circ$. Figure 1 shows Faraday rotation of the source G48.561–0.364 with $RM = 2396 \pm 8 \text{ rad m}^{-2}$. The Stokes Q and U spectra are well fitted by a model that depolarizes gradually to zero on the long-wavelength side of the band. RM Synthesis shows a distinct peak and RM

¹ <https://github.com/CIRADA-tools/RM>

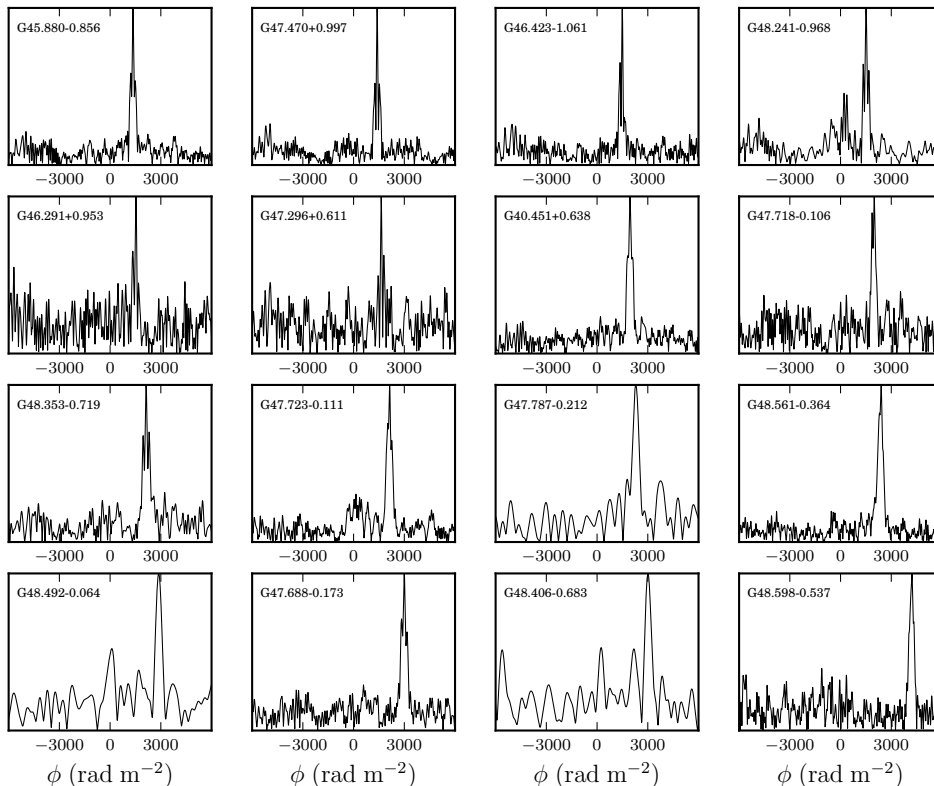


Figure 2. Faraday depth spectra before RM clean for the 16 sources with the highest RM , sorted in reading order by increasing RM . The spectra are normalized to the peak of the Faraday depth spectrum and show the search range -6000 rad m^{-2} to 6000 rad m^{-2} .

Clean components spread in a range that reflects the gradual depolarization at longer wavelengths. Complex Faraday rotation and occasional high RM s in extragalactic sources are seen across the sky and believed intrinsic to the source (e.g. O’Sullivan et al. 2017). We adopt the location of the peak of $|\tilde{\mathcal{F}}|$ as the Rotation Measure (RM), and identify it with the Faraday depth of the Galaxy (Equation 1). The value of the peak is the polarization degree of the source expressed as a percentage of Stokes I . This is consistent with previous surveys that had a smaller bandwidth. The RM s derived from RM synthesis are in general closely consistent with those derived from QU fitting. Figure 2 shows Faraday depth spectra before RM Clean for the 16 sources with the highest RM . Table 1 lists all detections that have $RM > 1000 \text{ rad m}^{-2}$. The complete sample is available in the on-line material.

Figure 3 shows RM as a function of Galactic longitude. We see a spike in Faraday rotation near $\ell \approx 48^\circ$, in the longitude range of the Sgr arm tangent (Georgelin & Georgelin 1976; Beuermann et al. 1985; Beuther et al. 2012; Vallée 2014). In the range $47^\circ < \ell \leq 49^\circ$, the mean RM is $\langle RM \rangle = 1.63 \times 10^3 \text{ rad m}^{-2}$ with standard deviation $\sigma_{RM} = 1.0 \times 10^3 \text{ rad m}^{-2}$ (23 sources). For $\ell > 49^\circ$ we find only one $RM >$

800 rad m^{-2} and a mean $\langle RM \rangle = 4.19 \times 10^2 \text{ rad m}^{-2}$ and $\sigma_{RM} = 2.4 \times 10^2 \text{ rad m}^{-2}$ (29 sources), while we find many times $RM > 800 \text{ rad m}^{-2}$ for $\ell < 47^\circ$ with a mean $\langle RM \rangle = 6.45 \times 10^2 \text{ rad m}^{-2}$ and $\sigma_{RM} = 3.9 \times 10^2 \text{ rad m}^{-2}$ (75 sources). Subtracting the mean $\langle RM \rangle$ for $49^\circ < \ell < 52^\circ$ as an estimate of the Faraday depth of the remainder of the Galaxy (c.f. models in Van Eck et al. 2011), the Sgr arm tangent contributes $\langle RM \rangle = (1.2 \pm 0.2) \times 10^3 \text{ rad m}^{-2}$, with standard deviation $\sigma_{RM} \approx 1.0 \times 10^3 \text{ rad m}^{-2}$. Several degrees from the tangent, the Sgr arm still adds $\sim 200 \text{ rad m}^{-2}$ in the mean and significant scatter to the total Galactic Faraday depth. The ratio $\langle RM \rangle / \sigma_{RM} \approx 1.7$ for each of the three regions. This may indicate anisotropy in the random component of the magnetic field (e.g. Brown & Taylor 2001; Beck 2015).

We find good agreement for the sources measured by Van Eck et al. (2011) that lie within the THOR survey (large red dots in Figure 3). Many of our RM s are significantly higher than the range $-129 \text{ rad m}^{-2} < RM < 831 \text{ rad m}^{-2}$ in Van Eck et al. (2011). The highest RM s in THOR are well above the threshold for bandwidth depolarization in the NVSS (Condon et al. 1998) from which their sample was selected. The green curve in Figure 3 shows the prediction of Galactic Faraday depth

from [Oppermann et al. \(2015\)](#), and the cyan curve shows the prediction from [Hutschenreuter & Ensslin \(2019\)](#) that includes free-free emission as a prior for Faraday depth amplitude. The THOR RM s indicate that the Galactic Faraday depth is significantly higher than previously realized. This part of the Galactic plane is outside the survey of [Schnitzeler et al. \(2019\)](#), but these authors also applied a threshold $|RM| < 1000 \text{ rad m}^{-2}$ in their sample selection.

Figure 3 (right) shows the distribution of pulsar DM s in our (ℓ, b) range. There appears to be a discontinuity in DM between the highest DM pulsars and the remainder of the sample, up to 300 pc cm^{-3} around $\ell \approx 48^\circ$, although the number of pulsars is small. If the two are related, the mean $\langle RM \rangle \approx 10^3 \text{ rad m}^{-2}$ and the $\Delta DM \approx 300 \text{ pc cm}^{-3}$ suggest a mean magnetic field $B_{\parallel} = 4 \pm 1 \mu\text{G}$. The statistical error assumes 20% uncertainty in both $\langle RM \rangle$ and ΔDM . A higher density of low-latitude pulsars is required for further investigation. [Han et al. \(2018\)](#) analysed pulsars with $|b| < 8^\circ$ and $45^\circ < \ell < 60^\circ$. These pulsars show a more continuous distribution of DM , and a mean field $B_{\parallel} = 1.4 \pm 1.0 \mu\text{G}$.

Our highest RM values exceed those published for sources behind Galactic H II regions. [Vallée & Bignell \(1983\)](#), [Purcell et al. \(2015\)](#), and [Ma et al. \(2019\)](#) reported $|RM|$ up to 633 rad m^{-2} behind the Gum nebula. [Harvey-Smith et al. \(2011\)](#) found $|RM| \lesssim 300 \text{ rad m}^{-2}$ behind a sample of large-diameter, high-latitude, H II regions. [Savage et al. \(2013\)](#) and [Costa et al. \(2016\)](#) found $|RM|$ up to 1383 rad m^{-2} behind the Rosette Nebula. The massive star formation region W4 ([Gray et al. 1999](#); [Costa & Spangler 2018](#)) and the Cygnus X region ([Brown et al. 2003](#)) have $|RM|$ up to 1500 rad m^{-2} . Some of these studies are directly or indirectly subject to the effects of bandwidth depolarization in the NVSS, which is known to list fewer polarized sources behind H II regions ([Stil & Taylor 2007](#)). Still, observations of Galactic H II regions to date show $|RM| \lesssim 1500 \text{ rad m}^{-2}$, with the high $|RM|$ confined to regions outlined by the thermal radio emission. Very strong Faraday rotation has been detected from pulsars near the Galactic centre, with $|RM|$ up to $6.7 \times 10^4 \text{ rad m}^{-2}$ ([Eatough et al. 2013](#); [Schnitzeler et al. 2016](#)), and $|RM|$ up to 5800 rad m^{-2} from the non-thermal filaments ([Lang et al. 1999](#); [Paré et al. 2019](#)). In the Galactic disk, two pulsars, PSR J1841–0500 ([Camilo et al. 2012](#)) and PSR J1839–0643 ([Han et al. 2018](#)) have $RM \approx -3000 \text{ rad m}^{-2}$, and the magnetar PSR J1550–5418 has $RM = -1860 \text{ rad m}^{-2}$.

In order to test whether the high RM s result from H II regions along the line of sight, their positions were cross matched with the catalog of Galactic H II regions of [Anderson et al. \(2014\)](#). This catalog is based on the mid-infrared WISE all sky survey, which provides a more

sensitive census of H II regions than the available radio continuum surveys. The $22 \mu\text{m}$ emission of stochastically heated small dust grains is spatially correlated with the ionized gas in an H II region ([Anderson et al. 2011](#)). The catalog is complete in the first quadrant for H II regions around a single star of spectral type O9.5 or earlier ([W. Armentrout et al. 2019](#), in preparation). Table 1 lists the H II region nearest to the line of sight selected by two criteria from the catalog of [Anderson et al. \(2014\)](#). The first listed H II region is the nearest considering the angular distance expressed in units of the H II region radius (d_1/R), and the second H II region is the nearest selected by angular distance only (d_2). For each case, the angular distance and the separation in terms of the H II region radius (R) is listed. We excluded the H II region G49.048–0.886, because it is not in the most recent version (2.2) of the on-line catalog².

Most high RM s are found away from detectable H II regions. Figure 4 shows RM s of extragalactic sources (+), pulsars (\times), and pulsar DM s (white squares) on a color-composite image of the Galactic plane that combines WISE $4.6 \mu\text{m}$, $12 \mu\text{m}$, and $22 \mu\text{m}$, MSX $8\mu\text{m}$, and THOR radio continuum images. H II regions appear as pink or bright yellow nebulae, while supernova remnants appear as blue nebulae. The highest RM is found on a line of sight that passes within $\sim 50 \text{ pc}$ from the star formation region W51, which is the 9th most luminous source of free-free emission in the Galaxy ([Rahman & Murray 2010](#)) at a distance of 5.4 kpc ([Sato et al. 2010](#)). The median $|RM|$ for 79 sources whose line of sight passes more than 2 times the radius R from the nearest H II region is 700 rad m^{-2} . This includes most of the high RM sources listed in Table 1. The median $|RM|$ for 14 sources whose line of sight passes within the radius of an H II region ($d_1 < R$) is 439 rad m^{-2} . The difference is hardly significant considering the sample size and the large scatter in RM . The RM spike is about a degree ($\approx 100 \text{ pc}$) from W51, on the inside of the spiral arm. This is upstream when considering the motion of gas and stars through the spiral arm.

4. DISCUSSION

The lack of correlation of high RM s with the H II region catalog of [Anderson et al. \(2014\)](#) indicates the high RM s arise in the more diffuse WIM. The excess RM s are all positive, indicating a mean magnetic field component toward the observer in the region in which they arise. Several of our RM s are significantly higher than RM s from star formation regions with strong thermal radio continuum emission. Emission from a Faraday rotating plasma may be unobservable if the plasma is spread out

² <http://astro.phys.wvu.edu/wise/>

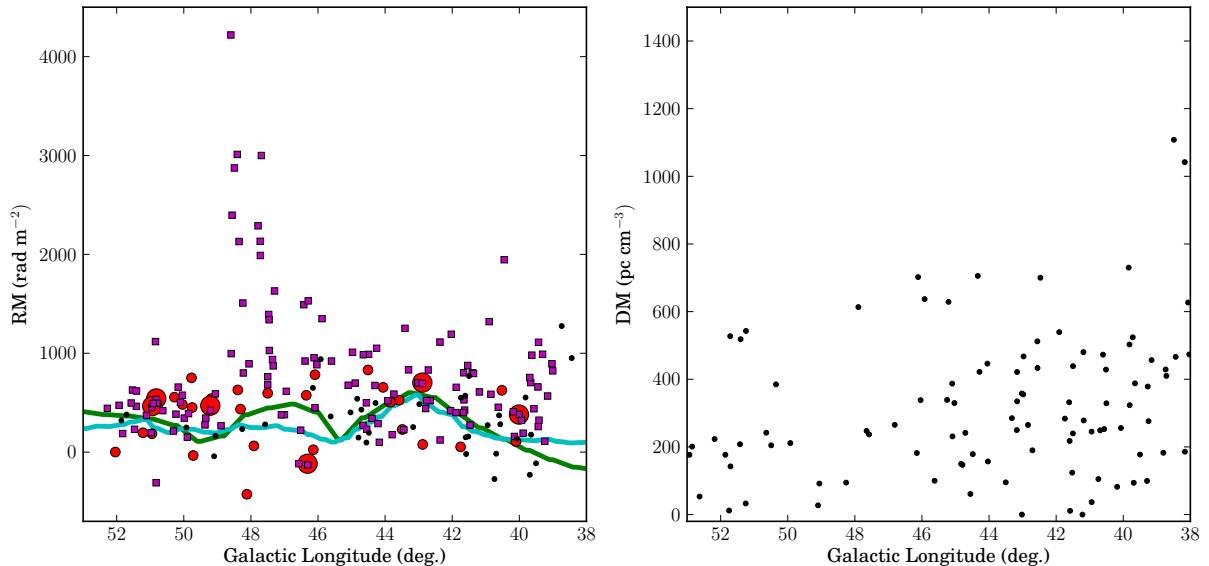


Figure 3. RM s (left) and pulsar DM s (right) in the range $39^\circ < \ell < 52^\circ$. The new THOR data are shown as magenta squares. Red dots indicate RM of extragalactic sources from Van Eck et al. (2011), with larger dots representing sources in the latitude range of THOR. The green curve shows Galactic RM predictions at $b = 0^\circ$ from Oppermann et al. (2015), and the cyan curve shows the same from Hutschenreuter & Ensslin (2019) for their model that includes free-free emission as a proxy of Faraday rotation amplitude. The black dots show data for pulsars in the THOR survey from the ATNF pulsar database (Manchester et al. 2005), updated on-line version <http://www.atnf.csiro.au/research/pulsar/psrcat>.

over a long distance along the line of sight, but a large RM from a region with small line-of-sight depth must result in a high emission measure unless the magnetic field strength is elevated. We consider two options: associate the RM spike at $\ell \approx 48^\circ$ with a confined region, e.g. the wall of a super bubble or an extended ionized halo around W51, with line-of-sight dimension $L \approx 100$ pc, or with the diffuse WIM in the spiral arm, with line-of-sight dimension $L \approx 1$ kpc. Within L we assume a filling factor of unity. A smaller filling factor would be equivalent to reducing L . As an order of magnitude estimate, we write $\langle RM \rangle \approx 0.81 n_e B_{\parallel} L \approx 10^3 \text{ rad m}^{-2}$ for $47^\circ < \ell < 49^\circ$. We focus the discussion on $\langle RM \rangle$, which includes several sources far from W51, noting that the extreme RM s near $\ell = 48^\circ.5$, $b = -0^\circ.6$ may be affected by W51 (compare Figure 4 with the radio recombination line map of W51 presented by Liu et al. 2019).

The case $L = 100$ pc then implies a mean $n_e B_{\parallel} \approx 10 \mu\text{G cm}^{-3}$. For a mean line-of-sight magnetic field $B_{\parallel} = 5 \mu\text{G}$, this implies $n_e \approx 2 \text{ cm}^{-3}$, and emission measure 400 pc cm^{-6} . The free-free emission from such a region would have a brightness temperature of 0.6 K at 1.4 GHz, for plasma temperature $T_e = 10^4$ K. The implied emission measure for the highest $RM \gtrsim 3000 \text{ rad m}^{-2}$ is an order of magnitude higher. We see structures on scales of $0^\circ.5$ with a contrast ~ 1 K in the THOR continuum image, but no excess that traces the higher RM s. On the other hand, free-free emission from super bubble walls is clearly detected around W4 (Costa & Spangler 2018) and W47 (Beuther et al. 2016). The high RM

sources of Costa & Spangler (2018), including *O10*, are enclosed by the contour $T_B = 5.7$ K, while the Galactic background is in the range 4.9 K to 5.1 K. Also, Gray et al. (1999) found that depolarization of diffuse emission is closely correlated with total intensity. A stronger mean magnetic field $B_{\parallel} \gtrsim 15 \mu\text{G}$ ($B_{\parallel} \gtrsim 45 \mu\text{G}$ for $RM \approx 3 \times 10^3 \text{ rad m}^{-2}$) would reduce the implied emission measure beyond detection in the radio continuum image. Although the mean $RM \approx 10^3 \text{ rad m}^{-2}$ at $\ell \approx 48^\circ$ is comparable to model predictions for super bubbles (Stil et al. 2009; Costa et al. 2016; Costa & Spangler 2018), the highest RM s are significantly larger.

If, however, the RM spike arises in the WIM of the Sgr arm with $L \approx 1$ kpc, the product $n_e B_{\parallel} \approx 1 \mu\text{G cm}^{-3}$. For mean $B_{\parallel} = 5 \mu\text{G}$, the implied electron density is $n_e = 0.2 \text{ cm}^{-3}$. This is an order of magnitude higher than the volume-average density of the WIM in the mid-plane (Gaensler et al. 2008), but less than $n_e \approx 0.9 \text{ cm}^{-3}$ reported by Langer et al. (2018) for compressed WIM in the Scutum spiral arm. Compression of the WIM in the spiral arm will also increase the magnetic field strength, so it is fair to say that $n_e \lesssim 0.2 \text{ cm}^{-3}$. The emission measure of this plasma $\lesssim 40 \text{ pc cm}^{-6}$ would be undetectable in the THOR continuum images. Association of the RM spike with compressed WIM in the Sgr arm also explains the difference in $\langle RM \rangle$ and σ_{RM} between $\ell > 49^\circ$, and $\ell < 47^\circ$ where the line of sight intersects the spiral arm. The line-of-sight component of the large-scale magnetic field may also be larger as a result of the compression of the plasma.

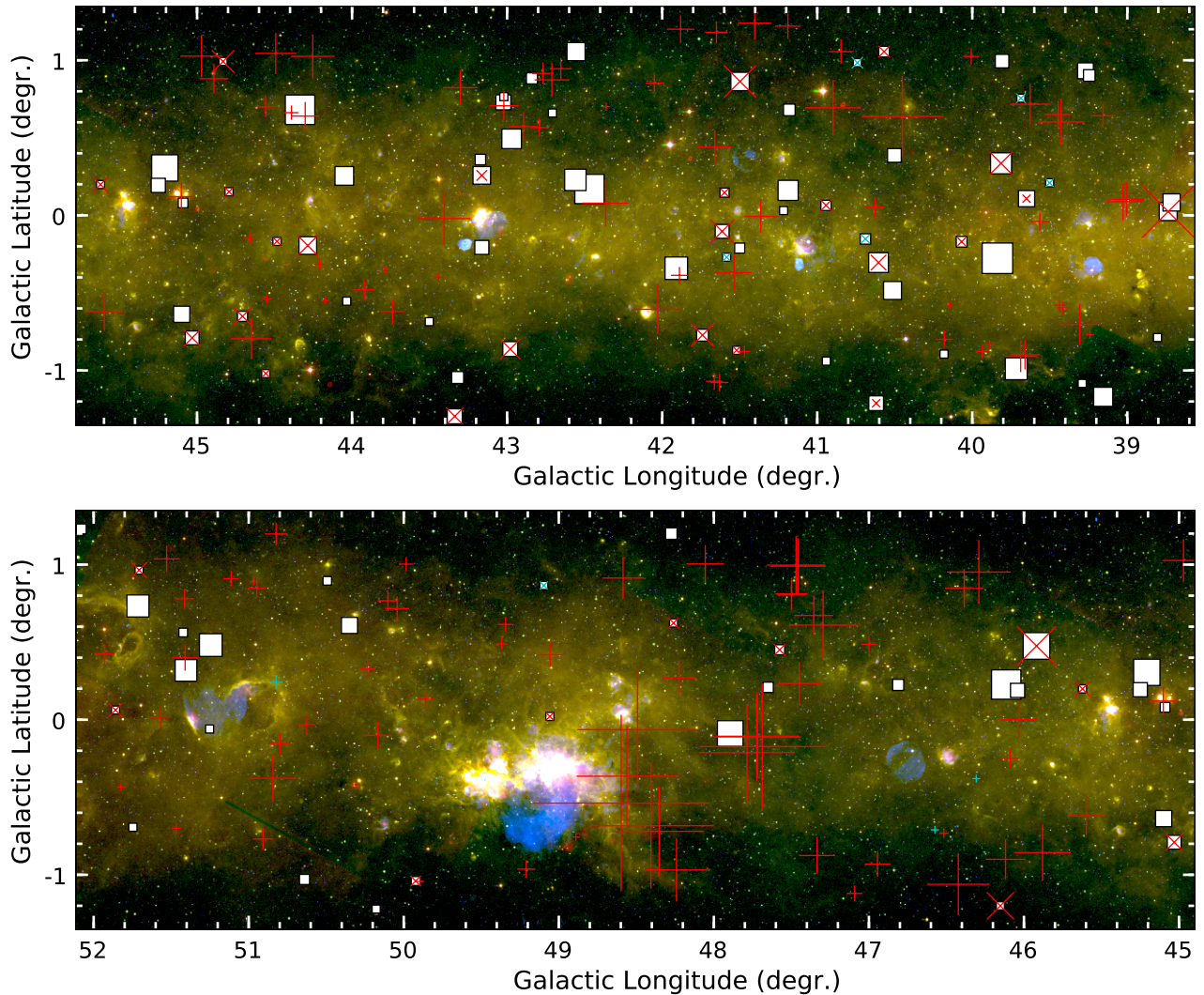


Figure 4. Section of the THOR survey in the region $39^\circ < \ell < 52^\circ$. The background image is a false-colour representation of MSX $8\mu\text{m}$, WISE $4.6\mu\text{m}$, $12\mu\text{m}$, $22\mu\text{m}$ and THOR + VGPS radio continuum. H II regions appear as pink or bright yellow nebulae, while supernova remnants appear as blue nebulae. Symbols indicate RM (+ for THOR extragalactic sources and \times for pulsars) with size proportional to $|RM|$ up to 4219 rad m^{-2} , with red indicating positive and cyan indicating negative RM . Pulsar DM s are indicated by white squares, scaled proportional to DM , with the largest squares indicating $DM \approx 650\text{ pc cm}^{-3}$ (see Figure 3). The THOR latitude range is within the 1.8 kpc scale height of the WIM (Gaensler et al. 2008) at any distance within the Milky Way.

The Sgr arm passes inside the solar circle and is known in the southern sky as the Carina arm (e.g. Georgelin & Georgelin 1976). Association of the RM spike with the spiral arm would be confirmed if a similar structure, with the sign of $\langle RM \rangle$ inverted, was found near the tangent of the Carina spiral arm around $\ell \approx 285^\circ$ (Vallée 2014). This area was previously covered by the Southern Galactic Plane Survey (SGPS, Haverkorn et al. 2006; Brown et al. 2007). The average SGPS RM at these longitudes is positive but close to zero (Brown et al. 2007), with a large range, $-547\text{ rad m}^{-2} < RM < 862\text{ rad m}^{-2}$. It is possible that a narrow region ($\Delta\ell \lesssim 2^\circ$) with excessive RM has eluded detection. The SGPS was observed with twelve 8 MHz channels between 1336

MHz and 1432 MHz (Haverkorn et al. 2006), frequencies where our high- RM sources depolarize in 8 MHz channels. The SGPS was also sensitive to diffuse Galactic emission that may have interfered with the detection of faint compact sources. Han et al. (2018) show pulsars for $|b| < 8^\circ$ near the Carina arm tangent with $-800\text{ rad m}^{-2} < RM < 900\text{ rad m}^{-2}$. A denser rotation measure grid is required to confirm or reject the presence of a negative RM spike near the Carina arm tangent.

We find that $\langle RM \rangle$ is $2.2 \times 10^2\text{ rad m}^{-2}$ (54%) higher and σ_{RM} is $1.5 \times 10^2\text{ rad m}^{-2}$ (63%) higher for $\ell \lesssim 47^\circ$ than for $\ell \gtrsim 49^\circ$. Such a sudden, substantial increase is not seen in current models of the magnetic field (e.g.

Van Eck et al. 2011), but it is far too extended to ascribe to a single H II region. If the Sgr arm raises the mean and the dispersion of RM for $\ell \lesssim 47^\circ$, we expect its effect to peak at the arm tangent ($47^\circ \lesssim \ell \lesssim 49^\circ$), where the line of sight through the arm is longest, and presumably aligned with the magnetic field. Association of the RM spike with an extended halo or bubble around W51 leaves unexplained why the RM is enhanced only on one side of W51, why we detect no excess thermal radio continuum from the direction of high RM s, and why $\langle RM \rangle$ and σ_{RM} are higher for $\ell \lesssim 47^\circ$. For these reasons, we favour association of the observed RM structure with the Sgr arm. This interpretation is consistent with the observation of polarized emission from the inside of spiral arms in galaxies with a strong spiral shock (Beck 2015, for a review), although these structures may be dominated by compressed turbulent field with little Faraday rotation (Fletcher et al. 2011).

This implies that Faraday rotation from spiral arms may be much stronger than previously thought, depending on the angle between the line of sight and the spiral arm. In particular, departures of the actual spiral arm from a perfect logarithmic spiral on kpc scales may impose systematic RM structure on scales of several degrees in Galactic longitude. The impact of the new RM data on the currently favoured model for the Galactic magnetic field by Jansson & Farrar (2012) cannot be determined without detailed modelling. The high Faraday depth of the arm suggests it needs to be known accurately to model the magnetic field in the remainder of the disk.

These results emphasize the importance of sensitivity to high $|RM|$. The initial polarization data product from the VLA Sky Survey (VLASS)³ is envisioned to be coarse cubes with 128 MHz channels. These cubes will have $\phi_{\max} = 2160 \text{ rad m}^{-2}$ at mid-band (3 GHz). Another consequence of high $|RM|$ associated with spiral arms is the potential effect on Faraday rotation of Fast Radio Bursts (FRBs, Lorimer 2018). An FRB was recently identified 4 kpc from the center of a luminous early type or lenticular spiral galaxy by Bannister et al. (2019). If these bursts are associated with neutron stars in young supernova remnants (e.g. Piro & Gaensler 2018), they may well be embedded in spiral arms. The results presented here suggest that some FRBs could have RM in the thousands from their host galaxy without the need to invoke an extreme environment.

5. CONCLUSIONS

We present first results from the THOR polarization survey of Faraday rotation of compact radio sources.

The THOR data reveal a strong spike in RM up to 4219 rad m^{-2} at the Sgr arm tangent, with several sources exceeding $2 \times 10^3 \text{ rad m}^{-2}$. On the low-longitude side, where the line of sight intersects the Sgr arm, the mean $\langle RM \rangle$ is higher by $2.2 \times 10^2 \text{ rad m}^{-2}$ (54%), and the standard deviation σ_{RM} is $1.5 \times 10^2 \text{ rad m}^{-2}$ (63%) larger than at higher longitude, where the line of sight does not intersect the Sgr arm. The combined pattern supports association of the RM spike with the large-scale structure of the spiral arm.

The strong Faraday rotation arises along lines of sight that do not intersect H II regions detected by WISE at $22 \mu\text{m}$. If the plasma is confined to any structure that has line-of-sight depth $L \approx 100 \text{ pc}$, e.g. the magnetized wall of a super bubble, its free-free emission should have been detected in the THOR continuum image unless the mean line-of-sight magnetic field $B_{\parallel} \gtrsim 15 \mu\text{G}$. We hypothesize that the RM spike arises from compressed magnetized WIM in the spiral arm, upstream from the major star forming regions. This hypothesis can be tested in the future because it implies a similar structure, with the sign of RM inverted, at the Carina arm tangent ($\ell \approx 285^\circ$) that may have eluded detection in existing surveys.

The excess Faraday depth of the Sgr arm tangent is several times the total Faraday depth of the remainder of the Milky Way disk. The arm acts as a very significant and structured Faraday screen inside the Galaxy. By inference, spiral arms in other galaxies may have similarly large Faraday depth. Some Fast Radio Bursts may have RM in the thousands without the need to invoke an extreme environment if these bursts are associated with neutron stars in spiral arms.

JMS acknowledges the support of the Natural Sciences and Engineering Research Council of Canada (NSERC), 2019-04848. HB, YW, and JS acknowledge support from the European Research Council under the European Community’s Horizon 2020 framework program (2014-2020) via the ERC Con-solidator Grant From Cloud to Star Formation (CSF)’ (project number 648505). HB and JS also acknowledge support from the Deutsche Forschungsgemeinschaft in the Collaborative Research Center (SFB 881) The Milky Way System (subproject B1). FB acknowledges funding from the European Unions Horizon 2020 research and innovation programme (grant agreement No 726384). RJS acknowledges an STFC Ernest Rutherford fellowship (grant ST/N00485X/1) and HPC from the Durham DiRAC supercomputing facility. SCOG and RSK acknowledge support from the Deutsche Forschungsgemeinschaft via SFB 881 (subprojects B1, B2, and B8) and from the Heidelberg cluster of excellence EXC 2181 STRUCTURES:

³ <https://science.nrao.edu/science/surveys/vlass>

A unifying approach to emergent phenomena in the physical world, mathematics, and complex data? funded by the German Excellence Strategy. This research was conducted in part at the Jet Propulsion Laboratory, which is operated by the California Institute of Technology under contract with the National Aeronautics and Space Administration (NASA). The National Radio

Astronomy Observatory is a facility of the National Science Foundation operated under cooperative agreement by Associated Universities, Inc. The authors acknowledge the use of the RMtools package written by Cormac Purcell. JMS thanks Y. K. Ma for his comments on the manuscript. The authors thank the anonymous referee for thoughtful comments on the manuscript.

REFERENCES

- Anderson, L. D., Bania, T. M., Balsler, D. S., et al. 2011, *ApJS*, 194, 32
- Anderson, L. D., Bania, T. M., Balsler, D. S., et al. 2014, *ApJS*, 212, 1
- Bannister, K. W., Deller, A. T., Phillips, C. et al. 2019, *Science*, 365, 565
- Beck, R. 2015, *A&A Rv*, 24, 4
- Beuermann, K., Kanbach, G., & Berkhuijsen, E. M. 1985, *A&A*153, 17
- Beuther, H., Tackenberg, J., Linz, H., et al. 2012, *ApJ*, 747, 43
- Beuther, H., Bihr, S., Rugel, M., et al. 2016, *A&A*, 595, A32
- Bihr, S., Johnston, K. G., Beuther, H., et al. 2016, *A&A*, 588, A97
- Brentjens, M. A., & De Bruyn, A. G. 2005, *A&A*, 441, 1217
- Brotten, N. W., MacLeod, J. M., & Vallee, J. P. 1988, *Ap&SS*, 141, 303
- Brown, J. C., & Taylor, A. R. 2001, *ApJ*, 563, L31
- Brown, J. C., Taylor, A. R., & Jackel, B. J. 2003, *ApJS*, 213, 223
- Brown, J. C., Haverkorn, M., Gaensler B. M., et al. 2007, *ApJ*, 663, 258
- Camilo, F., Ransom, S. M., Chatterjee, S., et al. 2012, *ApJ*, 746, 63
- Clegg, A. W., Cordes, J. M., Simonetti, J. H. et al. 1992, *ApJ*, 368, 143
- Condon, J. J., Cotton, W. D., Greisen, E. W., Yin, Q. F., Perley, R. A., Taylor, G. B., & Broderick, J. J. 1998, *AJ*, 115, 1693
- Cordes, J. M., Lazio, T. J. W. 2002, *arXiv:astro-ph/0207156*
- Costa, A. H., Spangler, S. R., Sink, J. R., et al. 2016, *ApJ*, 821, 92
- Costa, A. H., & Spangler, S. R. 2018, *ApJ*, 865, 65
- Dai, S., Johnston, S., Bell, M. E., et al. 2016, *MNRAS*, 462, 3115
- Eatough, R. P., Falcke, H., Karuppusamy, R., et al. 2013, *Nature*, 501, 391
- Ferrière, K. M., Mac Low, M.-M., Zweibel, E. G. 1991, *ApJ*, 375, 239
- Fletcher, A., Beck, R., Shukurov, A. et al. 2011, *MNRAS*, 412, 2396
- Gaensler, B. M., Madsen, G. J., Chatterjee, S., et al. 2008, *PASA*, 25, 184
- Georgelin, Y. M. & Georgelin, Y. P. 1976, *A&A*, 49, 57
- Gray, A. D., Landecker, T. L., Dewdney, P. E. et al. 1999, *ApJ*, 514, 221
- Harvey-Smith, L., Madsen, G. J., & Gaensler, B. M. 2011, *ApJ*, 736, 83
- Haverkorn, M., Gaensler, B. M., McClure-Griffiths, N. M., et al. 2006, *ApJS*, 167, 230
- Han, J. L., Manchester, R. N., Van Straten, W., et al. 2018, *ApJS*, 234, 11
- Heald, G. 2009, *IAUS*, 259, 591
- Heiles, C. & Haverkorn, M. 2012, *SSRv*, 166, 293
- Hutschenreuter, S., & Ensslin, T. A. 2019, *arXiv:1903.06735*
- Jansson, R. & Farrar, G. R. 2012, *ApJ*, 757, 14
- Klein, U. & Fletcher A. 2015, *Galactic and Intergalactic Magnetic Fields*, (Heidelberg:Springer)
- Klessen, R. S., & Glover, S. C. O. 2016, *Saas Fee Lecture Notes*, 43, 85
- Lang, C. C., Morris M., & Echevarria, L. 1999, *ApJ*, 526, 727
- Langer, W. D., Velusamy, T., Goldsmith, P. F. et al. 2018, *A&A*, 607, A59
- Law, C. J., Gaensler B. M., Bower, G. C., et al. 2011, *ApJ*, 728, 57
- Liu, B., Anderson, L. D., McIntyre, T. et al. 2019, *ApJS*, 240, 14
- Lorimer, D. R., *Nature Astronomy*, 2, 860
- Ma, Y. K., Mao, S. A., Stil, J. M., et al. 2019, *MNRAS*, 487, 3432
- Manchester, R. N., Hobbs, G. B., Teoh, A. et al. 2005, *AJ*, 129, 1993
- Oppermann, N., Janklewitz, H., Robbers, G., Bell, M. R., Ensslin, T. A., et al. 2012, *A&A*, 542, A93
- Oppermann, N., Janklewitz, H., Greiner, M. et al., 2015, *A&A*, 575, A118
- O’Sullivan, S. P., Purcell, C. R., Anderson, C. S. et al. 2017, *MNRAS*, 469, 4034
- Paré, D. M., Lang, C. C., Morris, M. R. et al. 2019, *arXiv:1909.08268*
- Piro, A. L., & Gaensler, B. M. 2018, *ApJ*, 861, 150
- Purcell, C. R., Gaensler, B. M., Sun, X. H. et al. 2015, *ApJ*, 804, 22
- Pratley, L. & Johnston-Hollitt, M. 2019, *arXiv:1906.00866*
- Reich, W., Reich, P., & Fürst 1990, *A&AS*, 83, 539
- Rahman, M., & Murray, N. 2010, *ApJ*, 719, 1104
- Sato, M., Reid, M. J., Brunthaler, A., et al. 2010, *ApJ*, 720, 1055
- Savage, A. H., Spangler, S. R., & Fisher, P. D. 2013, *ApJ*, 765, 42
- Schnitzeler, D. H. F. M., Eatough, R. P., Ferrière, K., et al. 2016, *MNRAS*, 459, 3005
- Schnitzeler, D. H. F. M., Carretti, E., Wieringa, M. H., et al. 2019, *MNRAS*, 485, 1293
- Sokoloff, D. D., Bykov, A. A., Shukurov, A., et al. 1998, *MNRAS*, 299, 189
- Stil, J. M., Taylor, A. R., Dickey, J. M., et al. 2006, *AJ*, 132, 1158
- Stil, J. M., & Taylor, A. R. 2007, *ApJL*, 663, 21
- Stil, J. M., Wityk, N., Ouyed, R., et al. 2009, *ApJ*, 701, 330
- Taylor, J. H., & Cordes, J. M. 1993, *ApJ*, 411, 674
- Taylor, A. R., Stil, J. M., & Sunstrum, C. 2009, *ApJ*, 702, 1230
- Tomisaka, K. 1998, *MNRAS*, 298, 797
- Uyaniker, B., Landecker, T. L., Gray, A. D., et al. 2003, *ApJ*, 585, 785
- Vallée, J. P., & Bignell, R. C. 1983, *ApJ*, 272, 131
- Vallée, J. P., Simard-Normandin M., & Bignell, R. C. 1988, *ApJ*, 331,321
- Vallée, J. P. 2014, *ApJS*, 215, 1
- Van Eck, C., Brown, J. C., Stil, J. M., et al. 2011, *ApJ*, 728, 97
- Wang, Y., Bihr, S., Rugel, M. et al. 2018, *A&A*, 619, A124

Table 1. Sources with RM in excess of 1000 rad m^{-2}

Name	S_{int} (mJy)	α	Π_0 (%)	RM (rad m^{-2})	Nearest H II (relative to size)	d_1 (')	d_1/R	Nearest H II (absolute)	d_2 (')	d_2/R
G39.427+0.603	43.6	-0.81	3.98	1111 ± 4	G39.515+0.511	7.6	0.9	G39.491+0.676	5.9	11.4
G40.451+0.638	20.1	-1.25	7.98	1946 ± 6	G40.154+0.648	17.8	1.1	G40.430+0.697	3.8	4.1
G40.898+0.694	90.3	-1.23	2.09	1320 ± 10	G40.154+0.648	44.7	2.7	G41.042+0.306	24.8	12.8
G42.028-0.605	424.7	-1.01	3.29	1192 ± 2	G42.006-0.500	6.4	0.7	G42.103-0.623	4.7	1.4
G42.365+0.079	144.7	-0.81	2.05	1113 ± 2	G42.562-0.107	16.3	2.5	G42.204+0.038	10.0	2.5
G43.407-0.021	64.0	-1.04	5.45	1252 ± 4	G43.617+0.059	13.5	3.8	G43.516+0.018	7.0	46.4
G44.253+1.026	38.7	-0.38	3.82	1050 ± 4	G43.999+0.978	15.4	6.7	G43.999+0.978	15.4	6.7
G44.971+1.027	129.2	-0.77	3.00	1010 ± 2	G6.404+22.865 ^a	2600	8.4	G45.197+0.740	21.9	16.4
G45.880-0.856	38.6	-0.99	10.61	1350 ± 2	G46.253-0.585	27.7	4.7	G45.992-0.511	21.8	21.4
G46.291+0.953	22.1	-0.92	3.07	1530 ± 13	G46.392+0.861	8.2	2.9	G46.375+0.896	6.1	15.1
G46.423-1.061	111.8	-0.96	3.23	1491 ± 5	G46.253-0.585	30.3	5.1	G46.325-0.790	17.3	16.7
G47.296+0.611	48.2	-1.12	2.82	1630 ± 9	G46.792+0.284	36.0	2.9	G47.094+0.492	14.0	14.0
G47.449+0.234	110.9	-0.89	1.67	1028 ± 7	G47.458+0.225	0.8	0.4	G47.458+0.225	0.8	0.4
G47.458+0.990	57.4	-1.08	6.90	1339 ± 1	G46.792+0.284	58.2	4.7	G47.765+1.424	31.9	30.9
G47.470+0.997	52.9	-1.13	11.94	1392 ± 1	G46.792+0.284	59.0	4.8	G47.765+1.424	31.1	30.1
G47.688-0.173	38.8	-0.55	3.01	3000 ± 9	G49.775-0.951	133.6	4.4	G47.580-0.075	8.8	6.9
G47.718-0.106 ^b	52	...	2.31	1989 ± 19	G49.775-0.951	133.4	4.4	G47.580-0.075	8.5	6.7
G47.723-0.111	207.6	-0.84	4.12	2132 ± 5	G49.775-0.951	133.0	4.4	G47.580-0.075	8.8	7.0
G47.787-0.212 ^c	32.8	-0.98	5.40	2289 ± 18	G49.775-0.951	127.2	4.2	G47.580-0.075	14.9	11.8
G48.241-0.968	460.9	-1.30	1.10	1508 ± 2	G49.775-0.951	92.0	3.1	G47.867-0.854	23.5	24.3
G48.353-0.719	90.2	-0.88	3.09	2130 ± 6	G49.775-0.951	86.4	2.9	G48.591-0.658	14.8	24.7
G48.406-0.683 ^c	35.2	-0.70	5.75	3011 ± 95	G49.775-0.951	83.7	2.8	G48.591-0.658	11.3	18.8
G48.492-0.064 ^c	44.7	-0.60	2.03	2874 ± 84	G48.599+0.044	9.2	2.3	G48.547-0.005	4.9	3.1
G48.561-0.364	126.2	-0.89	4.20	2396 ± 8	G48.871-0.383	18.7	2.1	G48.630-0.139	14.2	29.3
G48.598-0.537	92.0	-0.60	1.62	4219 ± 15	G48.871-0.383	18.9	2.2	G48.591-0.658	7.2	12.0
G50.844-0.377	64.5	-0.73	4.04	1118 ± 6	G51.010+0.060	28.0	1.7	G50.848-0.170	12.4	12.6

^aThis is the H II region around ζ Oph. H II regions closer to this RM have small angular size.

^bThis is a polarized component of a resolved source listed in the THOR catalog as G47.723 - 0.111. It is not well separated in total intensity.

^cSource detected in the full spectral resolution cube with 2 MHz channels (1.6 GHz - 1.9 GHz). Percent polarization for reference frequency 1.8 GHz. The RM error for these sources is larger mainly because of the reduced λ^2 range of the full-resolution search.

NOTE— Table 1 is published in its entirety in the machine-readable format. The sub-set of sources with $RM > 1000 \text{ rad m}^{-2}$ is shown here to support the discussion in the text. Column description: THOR name from the compact source catalog, flux density, spectral index, percent polarization at reference frequency 1.6 GHz unless noted otherwise, RM , name of nearest H II region, selected by angular distance in units of its radius, angular distance in arcminutes, angular distance in units of H II region radius, name of the nearest H II region selected by angular distance, angular distance in arcminutes, and angular distance in units of H II region radius.